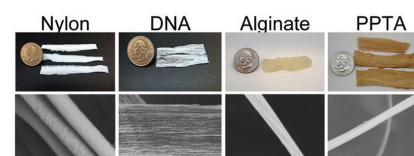


Production of Synthetic, Para-Aramid and Biopolymer Nanofibers by Immersion Rotary Jet-Spinning

Grant M. Gonzalez, Luke A. MacQueen, Johan U. Lind, Stacey A. Fitzgibbons, Christophe O. Chantre, Isabelle Huggler, Holly M. Golecki, Josue A. Goss, Kevin Kit Parker*

Nanofiber production platforms commonly rely on volatile carrier solvents or high voltages. Production of nanofibers comprised of charged polymers or polymers requiring nonvolatile solvents thus typically requires customization of spinning setup and polymer dope. In severe cases, these challenges can hinder fiber formation entirely. Here, a versatile system is presented which addresses these challenges by employing centrifugal force to extrude polymer dope jet through an air gap, into a flowing precipitation bath. This voltage-free approach ensures that nanofiber solidification occurs in liquid, minimizing surface tension instability that results in jet breakup and fiber defects. In addition, nanofibers of controlled size and morphology can be fabricated by tuning spinning parameters including air gap length, spinning speed, polymer concentration, and bath composition. To demonstrate the versatility of our platform, para-aramid (e.g., Kevlar) and biopolymer (e.g., DNA, alginate) nanofibers are produced that cannot be readily produced using standard nanofiber production methods.



1. Introduction

Fibrous materials possess unique combinations of properties, such as pliability, toughness, and durability that make them an attractive material for various applications. Synthetic fiber production emerged in the 19th century and high-strength synthetic fibers such as nylon

and Kevlar were commercialized in the 1930s and 1970s, respectively.^[1,2] Today, synthetic fibers are widely used to reinforce composite building materials, tires, sporting equipment, and armor.^[3,4] High porosity fibrous scaffolds are used for filtration, sensors, and catalysis^[5] as well as for tissue engineering and regenerative medicine research.^[5–8] Since unique properties of fibrous materials derive from the high aspect ratios of fibers,^[9–11] recent efforts have focused on developing techniques for producing nanofibers with diameters less than 1 μm . Examples of commonly used nanofiber production techniques include self-assembly,^[12,13] phase separation,^[14] template synthesis,^[15] touch spinning,^[16] magnetospinning,^[17] fluidic spinning,^[18–20] electrospinning (ES),^[2] and rotary jet-spinning (RJS).^[21–24]

ES is a popular and versatile method for manufacturing polymer nanofibers.^[2,25] However, producing nanofibers

G. M. Gonzalez, Dr. L. A. MacQueen, Dr. J. U. Lind,
S. A. Fitzgibbons, C. O. Chantre, I. Huggler, H. M. Golecki,
J. A. Goss, Prof. K. K. Parker
Disease Biophysics Group
Wyss Institute for Biologically Inspired Engineering
John A. Paulson School of Engineering and Applied Sciences
Harvard University
Cambridge, MA 02138, USA
E-mail: kkparker@seas.harvard.edu

using highly charged polymers jets can be challenging due to electric field interference. For instance, ES of pure alginate^[26–28] or DNA^[29] dissolved in water, even into a precipitation bath, is hampered by interference from their polyelectrolyte backbones.^[25,26,28,30] Additionally, some non-charged polymers cannot be spun using common volatile solvents such as hexafluoroisopropanol (HFIP), requiring additives to facilitate fiber formation. For instance, the addition of salts has been critical to spin meta-aramid dopes.^[31–35] Moreover, polymer solution viscosity and solvent evaporation rate must be carefully balanced in order to overcome instabilities caused by surface tension. Unless these spinning conditions are nominal, the dominance of surface tension can create a high-energy Raleigh–Plateau instability that forces the polymer-jet to bead or break apart.^[21,36,37]

To facilitate fiber production from nonvolatile solvents and from polymers with charged groups, we developed immersion rotary jet-spinning (iRJS), a centrifugal dry-jet wet spinning platform. The iRJS is an evolution of our previously reported RJS platform wherein high centrifugal forces are applied to extrude polymer dopes into nanofiber forming jets.^[23,24] While the RJS relies on carrier solvent evaporation, the iRJS contains a vortex-controlled precipitation bath in which fiber solidification occurs. The precipitation bath chemically crosslinks or precipitates polymer nanofibers, removing the need for using volatile carrier solvents. By utilizing precipitation instead of evaporation, the iRJS allows the fabrication of a variety of polymer nanofibers that cannot be readily formed using conventional RJS and ES techniques. To demonstrate the broad applicability of the iRJS, we spun nanofibers using diverse material precursors that included poly (para-phenylene terephthalamide) (PPTA, brand names: Kevlar, Twaron), nylon, DNA, and alginate. For biological applications, we developed pure alginate and blended alginate–gelatin nanofibers for use as tissue scaffolds. Using Kevlar as a model high-strength material precursor, we controlled the mechanical properties of PPTA nanofiber sheets for future use in composite materials.

2. Results and Discussion

Nanofibers are produced by the iRJS platform by extruding a polymer solution through an orifice of a rotating reservoir by centrifugal forces (Figure 1a). During extrusion, the solution forms a jet and undergoes jet-elongation and polymer alignment as it travels through an adjustable air gap (Movie S1, Supporting Information). At the end of the air gap, the polymer jet enters a precipitating vortex bath where the carrier solvent diffuses out, nanofiber solidification occurs (Figure 1b), and nanofibers are collected, for instance, onto a rotating collector in the form of oriented sheets (Figure 1c–f).

The selection of an appropriate liquid for the precipitating bath is critical, as it must dissolve jet carrier solvent while simultaneously precipitating or crosslinking the fiber polymer. For example, we spun PPTA or nylon into water, DNA into ethanol, and alginate into an aqueous CaCl_2 solution (Figure 1g–i). The use of a precipitation bath reduces the tendency towards extruded polymer jet beading driven by the Raleigh–Plateau instability,^[36] which limits the parameter space of dry RJS^[21] or ES.^[2,37] Before skin formation or phase separation suppresses this hydrodynamic instability, the timescale of fiber beading (Figure 2a) is governed by $\tau \approx \frac{\mu}{\gamma}r$, where μ is the solvent viscosity, γ is the surface tension, and r is the jet radius. By spinning into a bath which is miscible with the carrier solvent but precipitates the polymer, the surface tension of the interface approaches zero, $\gamma \rightarrow 0$, increasing the timescale of bead formation, $\tau \rightarrow \infty$, (Figure 2b). As a result, iRJS fibers are bead-free (Figure 2b), provided that the air gap is sufficiently small, such that the polymer solution reaches the precipitating bath before beading occurs. To verify this mechanism, we compared the formation of nylon fibers in the RJS platform, which contains no precipitant liquid, to fibers spun into a variety of precipitant baths using the iRJS platform (Figure 2a). Using the RJS platform, we dissolved nylon in volatile hexafluoroisopropanol (HFIP) and spun fibers at 30k RPM. Under these conditions, nylon fibers formed solely through the evaporation of the volatile solvent showed significant beading (Figure 2a). In contrast, beading was not observed in fibers produced with the iRJS platform when a water precipitation bath was used (Figure 2b). Water was chosen for the precipitation bath because it is miscible with HFIP, resulting in negligible interfacial tension between the jet-bath interface. Notably, after adding 25% vol. ethanol to the water precipitation bath, beading was observed, as ethanol is non-miscible with HFIP, and thus increased interfacial tension. By further increasing ethanol content to 50%, severe beading and further defective morphologies were observed (Figure S1, Supporting Information).

While the precipitant bath influences fiber morphology, varying iRJS system parameters (speed, concentration, air-gap length) enables the production of fibers with tunable diameters. For the case of nylon fibers, average fiber diameter decreased with increasing air gap distance ($2 \text{ cm} < d < 6 \text{ cm}$) and extruder rotation speed ($15 \text{ kRPM} < \omega < 45 \text{ kRPM}$). In contrast, fiber diameter increased with increasing weight per volume solution concentration ($5\% \text{ w/v} < C < 20\% \text{ w/v}$). Within this parameter space, average nylon fiber diameters of 250 nm to 2.75 μm were produced (Figure 2c–e, Figure S2, Supporting Information).

Reconfiguration of the precipitating bath vortex and fiber collector allows production of nanofiber constructs in a variety of structural arrangements. For instance,

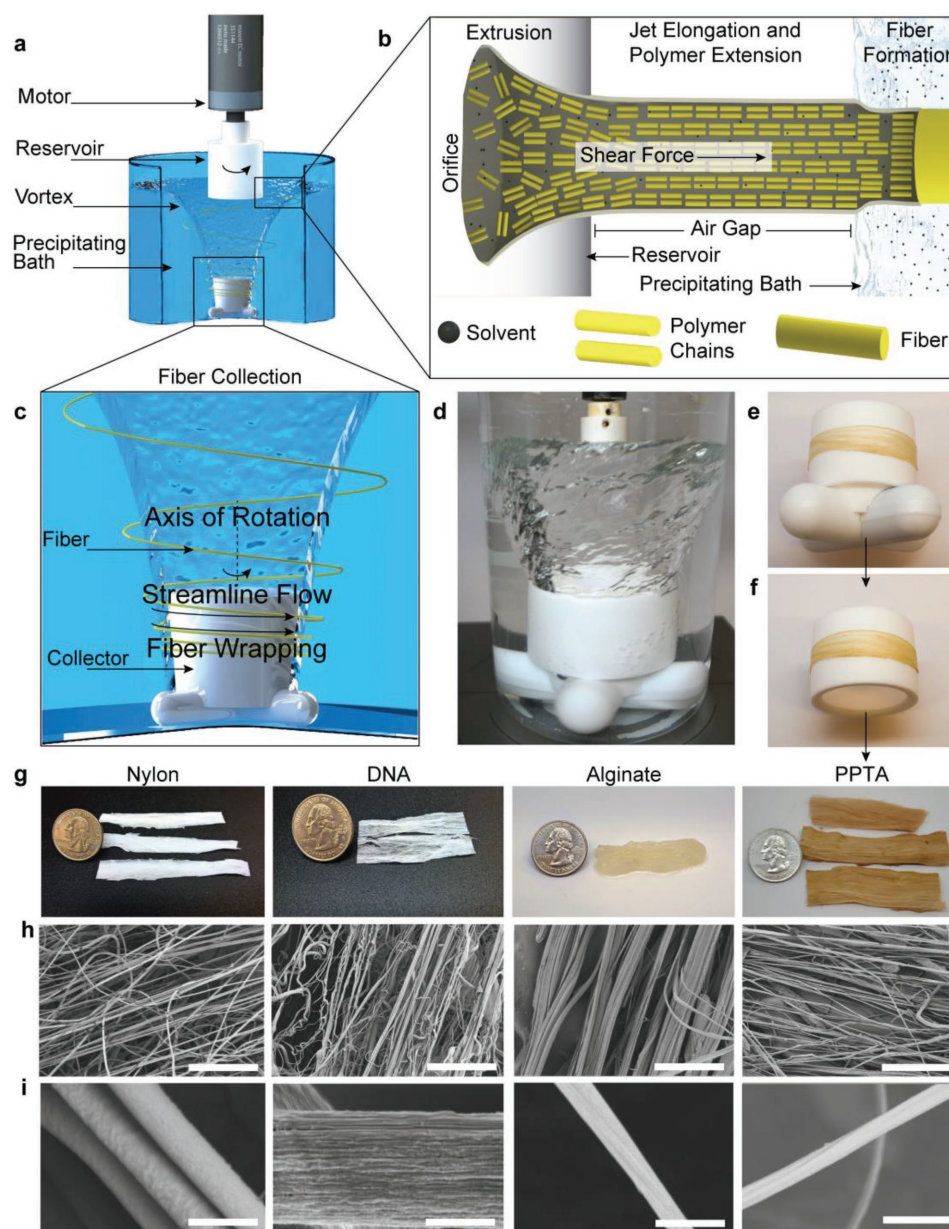


Figure 1. The immersion Rotary Jet-Spinning System (iRJS). a) The iRJS system controls the manufacturing of nanofibers by controlling the nanoscale properties, microscale assembly, and macroscale functionality. The iRJS spins a nanofiber solution through an orifice of a rotating reservoir. b) In an air gap, the polymer solution undergoes jet elongation, thinning while polymer chains align. After jet-elongation, the polymer solution enters the precipitating or crosslinking bath to form nanofibers. c) The streamlines of the vortex pull and collect the fibers onto the rotating collector. d) The iRJS system fabricates bulk nanofiber sheets around e) the collector with f) a removable sleeve. g) The polymer sheets were fabricated from nylon, biopolymers DNA and hydrated alginate in addition to synthetic PPTA after 30 s of spinning. These bulk sheets are comprised of h) nanofibers (scale bar = 40 μm) made from the i) following materials: nylon (scale bar = 500 nm), DNA (scale bar = 250 nm), alginate (scale bar = 1 μm), and PPTA (scale bar = 1 μm) as revealed by SEM images.

highly aligned anisotropic sheets are obtained by using a rotating drum collector (Figure 2d). We quantified the anisotropy of such sheets using an orientation order parameter^[38] (OOP) metric ($0 \leq \text{OOP} \leq 1$) with perfect alignment normalized to a value of one. The iRJS nanofiber sheets had OOP values approaching 1 ($\text{OOP} > 0.95$), indicating near perfect alignment

(Figure 2f–i). Nanofiber yarns can also be produced using a funnel collection method in place of a rotating collector (Figure S3, Supporting Information), applying a similar practice used in ES yarn collection systems.^[39–41] Finally, randomly oriented nanofibers can be achieved by adjusting the vortex to wrap the fibers above the collector (Figure S1, Supporting Information).

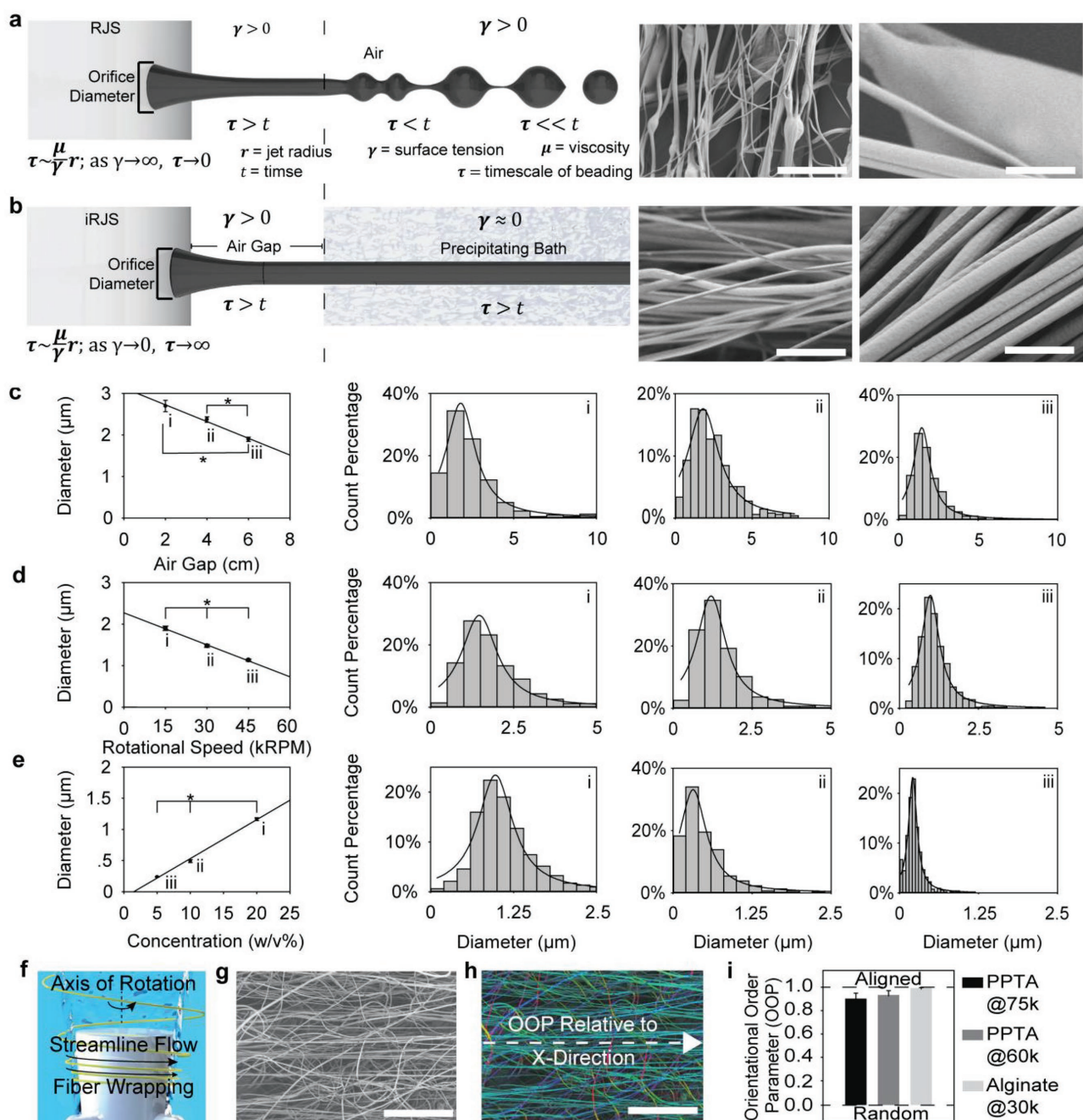


Figure 2. iRJS control over the morphology, diameter, and alignment of sheets. **a)** Traditional nanofiber spinning systems relying on volatile solvents cause beading as described by the Raleigh–Plateau instability and revealed in SEM images of nylon (left scale bar = 20 μm , right scale bar = 5 μm). **b)** Fibers spun with the iRJS system minimizes surface tension due to the precipitating bath, delaying Raleigh–Plateau instability to produce bead-free fibers as revealed by SEM images (left scale bar = 20 μm ; right scale bar = 5 μm). In addition to controlling fiber morphology, the iRJS controls fiber diameter by **c)** varying air-gap distance, **d)** rotation speed, and **e)** solution concentration ($n = 3$ production runs for each condition). For each mean fiber diameter, their corresponding distribution is plotted and denoted with roman numerals. The iRJS creates aligned sheets of these fibers by using the **f)** streamlines of the vortex to wrap the fibers around the collector. **g)** These resulting nanofiber sheets (scale bar = 100 μm) **h)** were measured by OOP corresponding angle-color image algorithms (scale bar = 100 μm). Across multiple spinning conditions, the iRJS nanofiber sheets are highly aligned as quantified in **i)** where 0 marks random order and 1 marks complete alignment. ($n = 3$ field of view for each spinning condition). Error bars are s.e.m., * $p < 0.05$.

The fabrication of biopolymer nanofibers for biomedical applications often requires the use of a nonvolatile aqueous carrier solvent. Using a precipitating solvent,

such as ethanol in the iRJS, DNA biopolymer nanofibers are produced using distilled water as a carrier solvent (Figure 1g–i). Additionally, aqueous precipitation baths

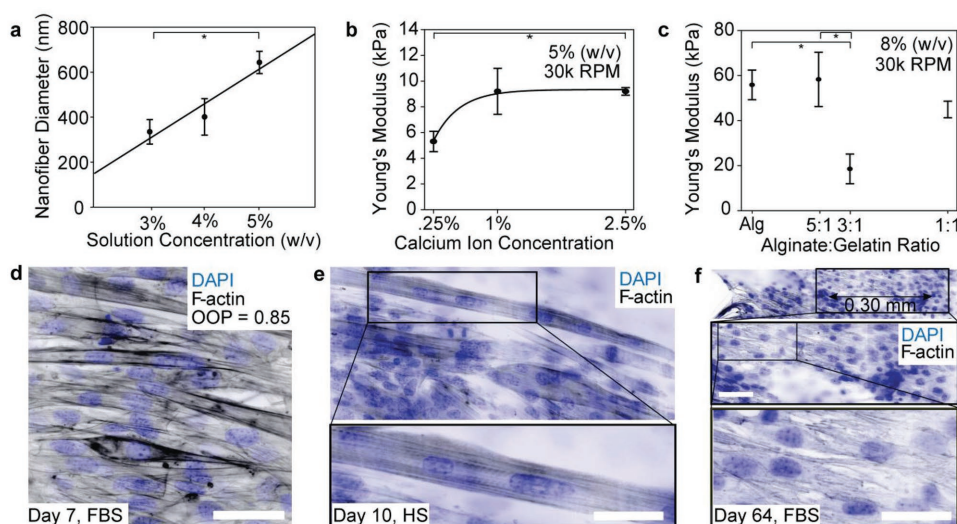


Figure 3. iRJS alginate–gelatin nanofiber scaffolds cultured with C2C12 myoblasts. a) Alginate nanofiber diameter depends on solution concentration ($n = 3$ production runs). b) Alginate nanofiber sheet mechanical strength depends on precipitation bath ion concentration ($n = 3$ for each condition). c) The cellular scaffolding Young's modulus depends on alginate–gelatin ratio ($n = 3$ for each condition). d) C2C12 myoblasts in 3D alginate–gelatin scaffolds with anisotropic orientation (scale bar = 20 μm). e) C2C12 maturation induced by culture in media supplemented with horse serum (HS) (scale bar = 20 μm). f) Long-term (64 d) C2C12 proliferation in an immature state using high concentration fetal bovine serum (15% FBS) (scale bars = 20 μm). DAPI and F-actin stains are shown with an inverted color-map to improve contrast. Error bars are s.e.m., * $p < 0.05$.

can be used by applying crosslinking agents to generate stable fibers. As an example, we used the iRJS to produce nanofibrous alginate scaffolds crosslinked in an aqueous CaCl_2 bath. Alginates are naturally occurring polysaccharides used in food products^[42,43] and for biomedical applications that benefit from alginate's biocompatibility, low toxicity, and mild gelation conditions.^[7] Medical uses of alginates include drug delivery vehicles^[44,45] and tissue engineering scaffolds,^[46,47] where cell-adhesive molecules are bound to alginate hydrogels to promote cell attachment.^[47] Although alginate nanofibers can be produced by ES, interference between the electric field and the alginate polyelectrolyte backbones^[25,26,28,30] must be overcome, for example, by spinning in a mixed glycerol–water solvent^[48] or by using a carrier polymer such as poly(ethylene oxide).^[26–28,49–52] Leveraging the ability of the iRJS to fabricate aligned nanofiber sheets, we produced alginate and blended alginate–bioprotein nanofibers, and explored their potential for skeletal muscle tissue engineering with tunable size and modulus (Figure 3a,b).

Tissue engineering scaffolds are designed to mimic properties of the extra cellular matrix in order to promote cell adhesion and guide tissue morphogenesis. Biocompatibility of naturally derived materials produced using nontoxic methods are advantageous because they can be more readily translated to clinical applications.^[7,8] Thus, we produced anisotropic nanofibrous scaffolds based on alginate blended with gelatin to promote cell adhesion. Gelation in CaCl_2 proved sufficient to produce nanofibers

from solutions in which the gelatin concentration was as high as 50%. By varying alginate–gelatin concentrations and subsequent gelatin crosslinking conditions, we produced scaffolds with elastic modulus values ranging between 5 and 60 kPa (Figure 3c). These values are comparable to native skeletal muscle (Supporting Information). In addition, our scaffolds were anisotropic (Figure 2f) and guided anisotropic cell assembly (Figure 3d–f). We seeded these scaffolds with C2C12 myoblasts and verified the scaffold's support of cell attachment, proliferation, and differentiation. C2C12 myoblasts could either be matured in situ, following ≈ 1 week of culture in differentiation media (Figure 3e), or could be maintained in their immature single nucleated state within these scaffolds for up to 2 months (Figure 3f). These experiments demonstrate that co-spinning alginate with cell-adhesive bioproteins (e.g., gelatin) provides a simple and effective means of producing blended alginate–bioprotein nanofibers. Similarly, through the inclusion of nutritional proteins in these nanofibers (Figure S4, Supporting Information), fibrous alginate scaffolds may achieve nutritional and medical goals while simultaneously enabling engineering of texture and taste, for future applications such as synthetic and cultured foods.^[53–55,79]

Beyond nanofiber production based on common carrier or aqueous solvents, the iRJS platform is well suited for the fabrication of polymer nanofibers that require the use of highly protic nonvolatile solvents. To demonstrate this, we applied the iRJS capabilities for spinning Kevlar-based para-aramid nanofibers, which mandates

that concentrated sulfuric acid is used as a carrier solvent. Poly(para-phenylene terephthalamide) (PPTA, the polymeric material of commercial Kevlar and Twaron) is a class of ultrastrong temperature-resistant paraaramids with broad uses that include ballistic apparel, brake and transmission friction parts, ropes and cables, and reinforcement of rubbers and other composites.^[4,56] Commercial PPTA fiber diameters are on the order of $\approx 10\text{ }\mu\text{m}$ and possess an inhomogeneous core-skin morphology that depends on proprietary production processes.^[57–60] Reducing fiber diameter will be of interest for use in composites, where the surface area-to-volume ratio of nanofibers can lead to improved adhesion to the matrix and strengthening of the composite.^[61,62] Production of PPTA nanofibers using ES has been described.^[63,64] However, complications with low and unreliable production yields have been reported.^[34,65,66] Alternative approaches to fabricate para-aramid nanofibers include chemical cross-linking of hydrolyzed or monomeric PPTA into short micron-long nanofibrils.^[67,68] In contrast, the iRJS is capable of higher throughput production of PPTA nanofibers with intact chemical structure.

Using the iRJS, we spun Kevlar dissolved in sulfuric acid at various concentrations into an aqueous precipitation bath. In the bath, sulfuric acid is diluted ≈ 1000 times and fibers solidified. To ensure that residue sulfuric acid did not degrade the nanofibers over time, we additionally washed the nanofiber fabrics with distilled water for 30 s followed by a 1 h drying step at $100\text{ }^{\circ}\text{C}$: The successful removal of sulfuric acid impurities was confirmed by energy-dispersive X-ray spectroscopy (EDS) (Figure S5, Supporting Information). Applying this procedure, we fabricated PPTA nanofibers with various diameters and tensile strength. Fiber diameter was controlled in the iRJS by adjusting polymer concentration and the shear forces applied via variable rotational speed. For 3% (wt/v%) polymer solutions, increasing spinning speed from 45 k RPM to 65 k RPM decreased nanofiber diameter from 1300 to 800 nm (Figure 4a). On the contrary, increasing concentration increased nanofiber diameter. Spun at 65 k RPM, PPTA concentrations of 1, 3, 5, or 10% (wt/v%) produced sheets of nanofibers with mean diameters of ≈ 500 , 800, 850, or 900 nm, respectively (Figure 4a–d).

To determine the mechanical properties of the PPTA nanofibers, we performed uniaxial tensile testing of macroscopic nanofiber sheets, spun at 65 k RPM at varying PPTA concentrations (Figure 4e–h). The 10% PPTA fiber sheets displayed the highest Young's modulus (Figure 4f). However, the 10% sample displayed lower ultimate tensile stress compared to the 5% sample (Figure 4g). Also, compared to higher PPTA concentrations, the PPTA nanofiber sheets spun from 3% precursor solutions had lower ultimate tensile stress and Young's modulus (Figure 4d).

All the macroscopic PPTA nanofiber sheets had lower Young's modulus and ultimate tensile stress compared to the reported values for Kevlar types 29 and 49.^[56,67] However, this apparent difference may be caused by uneven load distribution in the nanofibrous network.^[69,70] For instance, a 1000-fold difference in apparent Young's modulus has been reported for single PCL nanofibers, compared to values measured for macroscopic sheets composed of the same fibers.^[69] Assuming that the fibers of the anisotropic sheets span the entire sheet length, the toughness, the total amount of energy required to fracture all the fibers in the sample, whether in concert or one by one, will be less influenced by disorganization of the nanofiber sheets.^[71,72] To this point, the tensile toughness of the highly crystalline 5 and 10% nanofiber sheets were $81 \pm 20\text{ MPa}$ and $33 \pm 14\text{ MPa}$, respectively (Figure 4h), which is comparable to that of commercially available microfibers reported at 50 MPa.^[73] These findings are promising because high toughness is central to a wide range of high-performance material applications.^[56,73]

For commercial PPTA fibers, Young's modulus increases with increasing crystallinity while toughness decreases.^[3,4,74] To determine the relationship of PPTA nanofiber mechanics with crystallinity, we evaluated the local crystallinity of single PPTA nanofibers using transmission electron microscopy (TEM) (Figure 4i–l). The 3, 5, and 10% (wt/v%) precursor solutions spun at 65 k RPM all produced semicrystalline PPTA nanofibers (Figure 4m,n, Figure S6–12, Tables S1–4, Supporting Information) without a loss in the PPTA polymer bond chemistry (Figure S6, Supporting Information). For the 3% fibers, amorphous ring diffraction caused by randomly aligned polymer chains was dominant (Figure 4j), while for the 5 and 10% samples, discrete diffraction with high local band intensity was seen (Figure 4k,l), indicative of aligned polymer chains and crystalline domains. Furthermore, for the 10% sample, the meridial (002, 004, 006) and equatorial (010, 200, 210) diffraction bands along with a crystalline core and amorphous skin were observed (Figure S7iii,ix, Supporting Information). These variations follow the trend in Young's moduli observed in the mechanical tests of the 3, 5, and 10% samples, as increased crystalline morphology should lead to stiffer, more brittle fiber materials. Nevertheless, when investigating the bulk crystallinity of macroscopic fibrous sheets using Raman (Figure 4m,n) and FT-IR spectroscopy, we observed no quantifiable differences between the nanofibrous samples (Figure S7–12, Supporting Information). In these tests, all three nanofiber samples had comparable degrees of crystallinities which were higher than a cast film comparison, but significantly lower than that of a commercial Kevlar microfiber

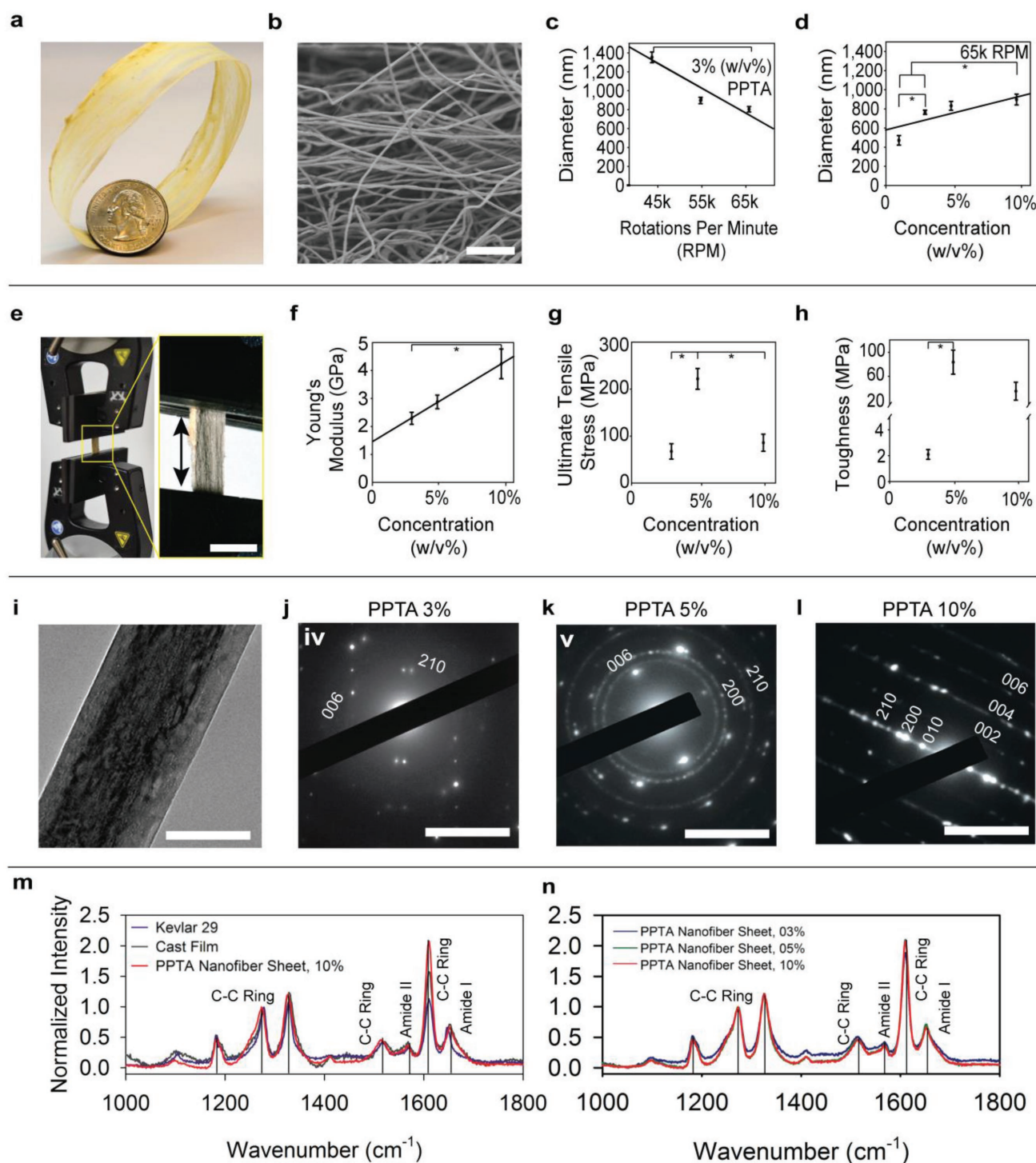


Figure 4. iRJS PPTA nanofiber sheets with control over nanofiber size and mechanical strength. **a)** PPTA sheets are composed of **b)** nanofibers (scale bar = 20 μm) with an average diameter dependent on **c)** spinning speed and **d)** polymer concentration. ($n = 3$ production runs). **e)** Uniaxial tensile testing was performed to determine the mechanics of fabricated PPTA sheets including **f)** Young's modulus, **g)** tensile stress, and **h)** toughness ($n = 3$ production runs). **i)** TEM imaging of the nanofibers (scale bar = 150 nm) allows for imaging of the selected area diffraction of the **j)** 3%, **k)** 5%, **l)** 10% PPTA nanofibers and designation of Miller Indices (scale bars = 5 nm^{-1}). **m)** Representative Raman spectrum of commercial Kevlar microfibers, cast film, and nanofiber sheets are graphed for comparison in addition to **n)** 3%, 5%, 10% PPTA nanofiber sheets spectra. Error bars are s.e.m., * $p < 0.05$.

reference (Figure S12, Supporting Information). This inconsistency between the local crystallinity as observed by TEM and the bulk measurements relying on Raman and FTIR spectroscopy, might arise from TEM imaging relying on fibers of diameters smaller than the average of the production run. It might also indicate that only local areas of increased crystallinity are present in the high concentration samples.

Nevertheless, the iRJS PPTA nanofibers possess potentials due to their small diameter. While commercial fiber diameters typically range from 10 to 20 μm ,^[56] the significantly smaller diameter of the iRJS PPTA nanofibers (500–1000 nm) provides a 10–20 times increase in surface area-to-volume ratio. For composite materials, the smaller diameter PPTA nanofibers may enhance fiber dispersion within matrix materials, increasing uniformity, minimizing local stress concentrations, and increasing the number of fibers available for bridging crack formations.^[75] Furthermore, the higher surface area-to-volume ratio of nanofibers can improve adhesion to the matrix, strengthening the composite^[61] as seen with other nanofiber composites^[9] with possible application towards composite materials for ballistic protection such as helmets.

3. Conclusions

The iRJS platform described here minimizes surface tension and fiber beading by spinning a polymer solution into a liquid bath. The bath chemically crosslinks or precipitates the polymer without the need for a volatile solvent. Adjusting the iRJS system parameters (air gap distance, rotational speeds, and solution concentration) enables control over nanofiber diameter. By avoiding the need for solvent evaporation and electric charge, the iRJS enables straightforward production of PPTA, nylon, DNA, and pure or blended alginate nanofiber sheets. Structural, mechanical, and biochemical properties of these nanofiber materials were controlled within the broad iRJS parameter space. Significantly, this wide range of nanofibrous materials was achieved without limiting production throughput.

4. Experimental Section

4.1. Design and Assembly of the iRJS

The iRJS system was custom built with the following parts: a 250 watt DC motor (35114, Maxon Precision Motors Inc., Fall River, MA) with variable speeds from 1000 to 80 000 RPMs, a motor control board (306089, Maxon Precision Motors Inc., Fall River, MA), a microcontroller (Arduino Due, Arduino LLC), and a potentiometer.

Changing the resistance of potentiometer changed the voltage supplied to and the speed of the motor. The rotating reservoir was custom manufactured from polysulfone or aluminum and included one 175 or 375 μm diameter orifice. The precipitating bath was contained in a 2L beaker or a custom-built polycarbonate container. A stir plate with variable power drove the stir bar and collector. The speed of the spinning reservoir ranged from 15 000 to 65 000 RPM, while collector speed was 350 RPM. The collector was machined from a rod of polytetrafluoroethylene (PTFE) into a cylinder with an opening for the stir bar. For the funnel collection system, precipitant was pumped into a funnel to create a vortex. For both collection methods, the air gap distance may be controlled independently by changing the height of reservoir relative to the vortex. The precipitating bath used is a miscible liquid to the solution solvent while not having the ability to solubilize the polymer. For example, nylon dissolved in hexafluoroisopropanol was spun into water, DNA dissolved in water into ethanol, alginate dissolved in water into calcium chloride solution, and PPTA dissolved in sulfuric acid into water.

4.2. Solution Preparation and Spinning

To make solutions of PPTA–sulfuric acid, PPTA (339741, McMaster-Carr, Elmhurst, IL) was dissolved into 99.999% sulfuric acid (339741, Sigma Aldrich, St. Louis, MO) and heated at 70 °C for 24 h or until dissolved. The PPTA–sulfuric acid solutions were spun at 70 °C and at variable speeds. Low viscosity alginate (A0682, Sigma Aldrich, St. Louis, MO) was used for measuring the effect of Ca^{2+} ion concentration on mechanical strength and alginate acid sodium salt (180947, Sigma Aldrich, St. Louis, MO) was used for cellular scaffolding to increase the mechanical strength of the alginate to more closely approximate skeletal muscle. To avoid gelation, alginate–gelatin solutions were spun at 60 °C and at 30k RPMs. Experimental procedures were carried out in a chemical hood to limit exposure to hazardous materials used in the fiber spinning process. If increasing concentration of carrier solvent diffusing into the bath hinders fiber formation, it is recommended to change the bath or utilize the funnel collection system to ensure fresh precipitant is used.

4.3. Scanning Electron Microscopy and Energy-Dispersive X-Ray Spectroscopy

A field emitting electron microscope (FESEM Supra 55VP, Zeiss, Oberkochen, Germany) was used at a voltage of 3kV to measure the diameter and to reveal the microscale assembly of the nanofibers. For sample preparation, 8 mm diameter samples were cut and adhered via carbon tape to 12 mm aluminum SEM stubs and then plated with a 10 nm coating of platinum/palladium (Pt/Pd) using a Quorum Sputter Coater (EMS 300T D, Quorum Technologies, Sussex, United Kingdom) to avoid charge build-up during imaging. Diameter measurements of nanofibers were done manually with ImageJ. Energy-dispersive X-ray spectroscopy (EDS) in the Zeiss SEM was performed in order to detect sulfuric acid impurities in the final nanofiber PPTA fabric. For EDS analysis, we used the same method as above for the SEM preparation minus the Pt/Pd coating. EDS was performed at 15kV energy to produce enough signal for detection.

4.4. Transmission Electron Microscopy

Transmission electron microscopy (TEM) was used to view the nanoscale features and crystallinity of the PPTA nanofibers. All TEM imaging was performed on a JEOL 2100 TEM (JEOL, Peabody, MA). Due to the small size of the fibers and the carbon content of the PPTA polymers, the PPTA nanofibers were imaged directly on a TEM sample grid at 80 kV. Miller Indexing of the diffraction patterns was determined using known lattice parameters ($a = .78$ nm, $b = .519$ nm, $c = 1.29$ nm) and crystal structure (orthorhombic).^[56,76] To ensure accuracy of measurements, the 80 kV diffraction patterns were calibrated using a known aluminum sample.

4.5. Tensile Testing

Uniaxial tensile testing was performed with a mechanical tester (5566, Instron, Norwood, MA). The end of PPTA nanofiber sheets was embed in epoxy and taped to avoid stress concentrations at the location of the clamp and sample interaction. Tests were performed under a constant strain rate of 500 mm min⁻¹ at a gauge length of 2 cm. The maximum strain rate was chosen to most closely replicate the mechanical environment of high performance applications. Young's modulus was calculated as the slope of stress-strain curve, ultimate tensile stress was calculated as the maximum value of the stress-strain curve, and toughness was calculated as the area underneath the stress-strain curve. The area occupied by the nanofibers in the sheets was calculated by measuring the area of the sheet and then subtracting the void space of the fibers based on density difference between the sheet and a single fiber. For PPTA nanofibers tested mechanically, fiber diameters ranged from 750 to 900 nm, density was .43 gm cm⁻³, and OOP values were .95 or greater. Mechanical testing of alginate-gelatin nanofibers after transglutaminase crosslinking (Modernist Pantry, Portsmouth, NH) crosslinking was obtained with a biaxial tension test (CellScale BioTester, Waterloo, Canada). For alginate nanofibers tested mechanically, fiber diameters ranged from 600 to 800 nm, density was 1.02 gm cm⁻³, and OOP values were .95 or greater.

4.6. Skeletal Muscle Cell Seeding and Culture

Alginate-gelatin produced scaffolding with post-processing transglutaminase (Modernist Pantry, Portsmouth, NH) was used as a cellular scaffolding. Mouse myoblast cell lines (C2C12, ATCC CRL-1772) were seeded at 50 000 cm⁻² and cultured in a growth medium of DMEM culture medium (11995-065, Gibco, Carlsbad, CA) supplemented with 15% fetal bovine serum (Invitrogen, Carlsbad, CA). C2C12 maturation medium was DMEM/F-12 (12-719F, Lonza, Walkersville, MD) supplemented with 5% horse serum (Gibco, Carlsbad, CA).

4.7. Fourier Transform Infrared (FT-IR) and Raman Spectroscopy

A Bruker FT-IR Microscope (Lumos, Bruker, Billerica, MA) was used in attenuated total reflection (ATR) mode to measure the infrared spectra of the nanofibers. Horiba Multiline Raman Spectrometer was used with a 633 nm laser and 1800 mm grating.

LabSpec 6 from Horiba was used to perform peak analysis and fitted to literature values.^[77,78]

4.8. Statistical Analysis

Nanofiber diameter and mechanical properties were evaluated using SigmaPlot software (v12.5, Systat Software Inc., San Jose, CA). Nylon size dependence (Figure 2c), fiber diameter versus polymer weight concentration (Figure 3a, Figure 4b) and fiber diameter versus rotations per minute (Figure 4a) failed the Shapiro-Wilk normality test, and thus were evaluated using Kruskal-Wallis one way analysis of variance on ranks using the Dunn's test for post hoc analyses. Mechanical data (Figure 3b,c, Figure 4d) passed the Shapiro-Wilk normality test and were thus compared using one-way ANOVA, and the Tukey test for post-hoc analysis. For all statistical analyses, p-values less than 0.05 were considered statistically significant.

Supporting Information

Supporting Information is available from the Wiley Online Library or from the author.

Acknowledgements: L.A.M. and J.U.L. contributed equally to this work. The authors thank Prof. Adrian Buganza for his contribution on the mechanics of nanofiber sheets, Dr. Sean Sheehy for his editorial contribution, and the John A. Paulson School of Engineering and Applied Sciences Scientific Instrument Shop at Harvard University for their manufacturing of reservoirs and collectors. This work was performed in part at the Center for Nanoscale Systems (CNS), a member of the National Nanotechnology Infrastructure Network (NNIN), which is supported by the National Science Foundation under NSF award no. 1541959. CNS is part of Harvard University. This research has been funded in part by subcontract #312659 from Los Alamos National Laboratory under a prime Defense Threat Reduction Agency grant DE-AC52-06NA25396; National Heart, Lung, and Blood Institute of the National Institutes of Health under Award Number U01HL100408; National Center For Advancing Translational Sciences of the National Institutes of Health under Award Number UH3TR000522; the Harvard Materials Research Science and Engineering Center under the NSF Award Number DMR-1420570; and the Harvard PSE Accelerator Fund. The content is solely the responsibility of the authors and does not necessarily represent the official views of the funding agencies and institutions.

Received: August 17, 2016; Published online: October 7, 2016;
DOI: 10.1002/mame.201600365

Keywords: alginate; immersion rotary jet-spinning; nanofibers; nanofiber production; para-aramid

- [1] C. V. Boys, *Proc. Phys. Soc., London* **1887**, 9, 8.
- [2] C. J. Luo, S. D. Stoyanov, E. Stride, E. Pelan, M. Edirisinghe, *Chem. Soc. Rev.* **2012**, 41, 4708.
- [3] M. Jassal, S. Ghosh, *Indian J. Fibre Text. Res.* **2002**, 27, 290.
- [4] D. Tanner, J. A. Fitzgerald, B. R. Phillips, *Adv. Mater.* **1989**, 5, 151.
- [5] V. Shabafrooz, M. Mozafari, D. Vashae, T. Lobat, *J. Nanosci. Nanotechnol.* **2014**, 14, 522.

- [6] J. Lannutti, D. Reneker, T. Ma, D. Tomasko, D. Farson, *Mater. Sci. Eng. C* **2007**, 27, 504.
- [7] K. Y. Lee, D. J. Mooney, *Prog. Polym. Sci.* **2012**, 37, 106.
- [8] C. Borselli, H. Storrie, F. Benesch-Lee, D. Shvartsman, C. Cezar, J. W. Lichtman, H. H. Vandenburgh, D. J. Mooney, *Proc. Natl. Acad. Sci. USA* **2010**, 107, 3287.
- [9] J. S. Kim, D. H. Reneker, *Polym. Compos.* **1999**, 20, 124.
- [10] Z. M. Huang, Y. Z. Zhang, M. Kotaki, S. Ramakrishna, *Compos. Sci. Technol.* **2003**, 63, 2223.
- [11] R. Vasita, D. S. Katti, *Int. J. Nanomed.* **2006**, 1, 15.
- [12] S. Paramonov, H.-W. Jun, J. Hartgerink, *J. Am. Chem. Soc.* **2006**, 128, 7291.
- [13] J. D. Hartgerink, E. Beniash, S. I. Stupp, *Science* **2001**, 294, 1684.
- [14] P. X. Ma, R. Zhang, *J. Biomed. Mater. Res.* **1999**, 46, 60.
- [15] C. Pang, G.-Y. Lee, T. Kim, S. Kim, H. Kim, S.-H. Ahn, K.-Y. Suh, *Nat. Mater.* **2012**, 11, 795.
- [16] A. Tokarev, D. Asheghali, I. M. Griffiths, O. Trotsenko, A. Gruz, X. Lin, H. A. Stone, S. Minko, *Adv. Mater.* **2015**, 27, 1.
- [17] A. Tokarev, O. Trotsenko, I. M. Griffiths, H. A. Stone, S. Minko, *Adv. Mater.* **2015**, 27, 3560.
- [18] P.-L. Josep, R.-M. Marta, U. Hartfelder, I. Imaz, D. Maspocho, P. S. Dittrich, *J. Am. Chem. Soc.* **2011**, 133, 4216.
- [19] M. Numata, Y. Takigami, M. Takayama, T. Kozawa, N. Hirose, *Chem.—A Eur. J.* **2012**, 18, 13008.
- [20] S. K. Smoukov, T. Tian, N. Vitchuli, S. Gangwal, P. Geisen, M. Wright, E. Shim, M. Marquez, J. Fowler, O. D. Velez, *Adv. Mater.* **2015**, 27, 2642.
- [21] H. M. Golecki, H. Yuan, C. Glavin, B. Potter, M. R. Badrossamay, J. A. Goss, M. D. Phillips, K. K. Parker, *Langmuir* **2014**, 30, 13369.
- [22] M. Badrossamay, K. Balachandran, A. K. Capulli, H. M. Golecki, A. Agarwal, J. A. Goss, H. Kim, K. Shin, *Biomaterials* **2014**, 35, 3188.
- [23] M. Badrossamay, M. Holly, J. A. Goss, K. Parker, *Nano Lett.* **2010**, 10, 2257.
- [24] P. Mellado, H. A. McIlwee, M. R. Badrossamay, J. A. Goss, L. Mahadevan, K. K. Parker, *Appl. Phys. Lett.* **2011**, 99, 203107.
- [25] J. D. Schiffman, C. L. Schauer, *Polym. Rev.* **2008**, 48, 317.
- [26] J.-W. Lu, Y.-L. Zhu, Z.-X. Guo, P. Hu, J. Yu, *Polymer* **2006**, 47, 8026.
- [27] C. A. Bonino, M. D. Krebs, C. D. Saquing, S. Jeong, K. L. Shearer, E. Alsberg, S. A. Khan, *Carbohydr. Polym.* **2011**, 85, 111.
- [28] C. D. Saquing, C. Tang, B. Monian, C. A. Bonino, J. L. Manasco, E. Alsberg, S. A. Khan, *Ind. Eng. Chem. Res.* **2013**, 52, 8692.
- [29] Y. Liu, J. Chen, V. Misoska, G. Wallace, *React. Funct. Polym.* **2007**, 67, 461.
- [30] S. Safi, M. Morshed, S. A. H. Ravandi, M. Ghiaci, *J. Appl. Polym. Sci.* **2007**, 105, 3245.
- [31] H. Oh, H. Pant, Y. Kang, K. Jeon, B. Pant, C. Kim, H. Kim, *Polym. Int.* **2012**, 61, 1675.
- [32] H. Oh, S. Han, S. Kim, *J. Polym. Sci., Part B: Polym. Phys.* **2014**, 52, 807.
- [33] J. M. D. T. S. Villar-Rodil, J. I. Paredes, A. Martínez-Alonso, *J. Therm. Anal. Calorim.* **2002**, 70, 37.
- [34] L. Yao, C. Lee, J. Kim, *Fibers Polym.* **2010**, 11, 1032.
- [35] W. Yang, H. Yu, M. F. Zhu, H. W. Bai, Y. M. Chen, *J. Macromol. Sci., Part B: Phys.* **2006**, 45, 573.
- [36] R. Mead-Hunter, A. J. C. King, B. J. Mullins, *Langmuir* **2012**, 28, 6731.
- [37] W. Zuo, M. Zhu, W. Yang, H. Yu, Y. Chen, Y. Zhang, *Polym. Eng. Sci.* **2005**, 45, 704.
- [38] A. Grosberg, P. L. Kuo, C. L. Guo, N. A. Geisse, M.-A. Bray, S. P. Sheehy, K. K. Parker, *PLoS Comput. Biol.* **2011**, 7, 1001088.
- [39] W. E. Teo, R. Gopal, R. Ramaseshan, K. Fujihara, S. Ramakrishna, *Polymer* **2007**, 48, 3400.
- [40] M. Yousefzadeh, M. Latifi, W. E. Teo, M. Amani-Tehran, S. Ramakrishna, *Polym. Eng. Sci.* **2011**, 51, 323.
- [41] M. Yousefzadeh, M. Latifi, M. Amani-Tehran, W.-E. Teo, S. Ramakrishna, *J. Eng. Fibers Fabr.* **2012**, 7, 17.
- [42] K. I. Draget, O. Smidsrød, S.-B. Skjåk-Broek, *Polysaccharides and Polyamides in the Food Industry, Properties, Production and Patents*, Wiley-VCH, Weinheim **2005**.
- [43] I. Brownlee, C. Seal, M. Wilcox, P. Dettmar, J. Pearson, *Alginates: Biology and Applications*, Springer, Berlin **2009**, pp. 211–228.
- [44] H. H. Tønnesen, J. Karlsen, *Drug Dev. Ind. Pharm.* **2002**, 28, 621.
- [45] X. Zhao, J. Kim, C. A. Cezar, N. Huebsch, K. Lee, K. Bouhadir, D. J. Mooney, *Proc. Natl. Acad. Sci. USA* **2011**, 108, 67.
- [46] C. K. Kuo, P. X. Ma, *Biomaterials* **2001**, 22, 511.
- [47] A. D. Augst, H. J. Kong, D. J. Mooney, *Macromol. Biosci.* **2006**, 6, 623.
- [48] H. Nie, A. He, J. Zheng, S. Xu, J. Li, C. C. Han, *Biomacromolecules* **2008**, 9, 1362.
- [49] N. Bhattarai, Z. Li, D. Edmondson, M. Zhang, *Adv. Mater.* **2006**, 18, 1463.
- [50] S. Jeong, M. D. Krebs, C. A. Bonino, S. A. Khan, E. Alsberg, *Macromol. Biosci.* **2010**, 10, 934.
- [51] G. Kim, K. Park, *Polym. Eng. Sci.* **2009**, 49, 2242.
- [52] C. A. Bonino, K. Efimenko, S. Jeong, M. D. Krebs, E. Alsberg, S. A. Khan, *Small* **2012**, 8, 1928.
- [53] W. Churchill, *Thoughts and Adventures*, Thornton Butterworth, London **1932**.
- [54] M. L. Langelaan, K. J. Boonen, R. B. Polak, F. P. Baaijens, M. J. Post, D. W. van der Schaft, *Trends Food Sci. Technol.* **2010**, 21, 59.
- [55] M. J. Post, *Meat Sci.* **2012**, 92, 297.
- [56] H. H. Yang, *Kevlar Aramid Fiber*, Wiley, Richmond, VA, USA **1993**.
- [57] S. L. Kwolek, P. W. Morgan, J. R. Schaefgen, L. W. Gulrich, *Macromolecules* **1977**, 10, 1390.
- [58] S. Roth, M. Burghammer, A. Janotta, C. Riekel, *Macromolecules* **2003**, 36, 1585.
- [59] D. Xu, K. Okuyama, F. Kumamaru, M. Takayangi, *Polym. J.* **1984**, 16, 31.
- [60] J. Wollbrett-Blitz, S. Joannès, R. Bruant, C. Le Clerc, M. Romero De La Osa, A. Bunsell, A. Marcellan, *J. Polym. Sci., Part B: Polym. Phys.* **2016**, 54, 374.
- [61] J. Kalantar, L. T. Drzal, *J. Mater. Sci.* **1990**, 25, 4186.
- [62] J. Kim, D. H. Reneker, *Polym. Compos.* **1999**, 20, 124.
- [63] G. Srinivasan, D. H. Reneker, *Polym. Int.* **1995**, 36, 195.
- [64] J. Yao, J. Jin, E. Lepore, N. M. Pugno, C. W. M. Bastiaansen, T. Peijs, *Macromol. Mater. Eng.* **2015**, 300, 1238.
- [65] Y. Park, J. Lee, Y. Nam, W. Park, *J. Appl. Polym. Sci.* **2015**, 132, 41515.
- [66] J. Yao, C. Bastiaansen, T. Peijs, *Fibers* **2014**, 2, 158.
- [67] K. Cao, C. P. Siepermann, M. Yang, A. M. Waas, N. A. Kotov, M. D. Thouless, E. M. Arruda, *Adv. Funct. Mater.* **2013**, 23, 2072.
- [68] H. Yan, J. Li, W. Tian, L. He, X. Tuo, T. Qiu, *RSC Adv.* **2016**, 6, 26599.
- [69] F. Croisier, A. S. Duwez, C. Jerome, A. F. Leonard, K. O. Van Der Werf, P. J. Dijkstra, M. L. Bennink, *Acta Biomater.* **2012**, 8, 218.
- [70] C. L. Pai, M. C. Boyce, G. C. Rutledge, *Polymer* **2011**, 52, 6126.

- [71] U. Stachewicz, I. Peker, W. Tu, A. H. Barber, *ACS Appl. Mater. Interfaces* **2011**, 3, 1991.
- [72] C. T. Koh, D. G. T. Strange, K. Tonsomboon, M. L. Oyen, *Acta Biomater.* **2013**, 9, 7326.
- [73] F. Vollrath, D. P. Knight, *Nature* **2001**, 410, 541.
- [74] Y. Rao, A. J. Waddon, R. J. Farris, *Polymer* **2001**, 42, 5937.
- [75] M. Vorechosky, V. Sadilek, R. Rypl, *Eng. Mech.* **2013**, 20, 3.
- [76] E. G. Chatzi, J. L. Koenig, *Polym.-Plast. Technol. Eng.* **1987**, 26, 229.
- [77] L. Penn, F. Milanovich, *Polymer* **1979**, 20, 31.
- [78] P. K. Kim, C. Chang, S. L. Hsu, *Polymer* **1986**, 27, 34.
- [79] I. Datar, M. Betti, *Innov. Food Sci. Emerg. Technol.* **2010**, 11, 13.